geosciences

MDPI

Article

The March 2021 Damasi Earthquake Sequence, Central Greece: Reactivation Evidence across the Westward Propagating Tyrnavos Graben

Ioannis K. Koukouvelas [1,*], Konstantinos G. Nikolakopoulos [1], Aggeliki Kyriou [1], Riccardo Caputo [2,3], Alexandros Belesis [4], Vasiliki Zygouri [1], Sotirios Verroios [1], Dionysios Apostolopoulos [1] and Ioannis Tsentzos [4]

1 Department of Geology, University of Patras, 26504 Patras, Greece; knikolakop@upatras.gr (K.G.N.); a.kyriou@upnet.gr (A.K.); zygouri@upatras.gr (V.Z.); verroios@upatras.gr (S.V.); apostolopoulos.dionysios@upatras.gr (D.A.)
2 Department of Physics and Earth Sciences, University of Ferrara, 44122 Ferrara, Italy; rcaputo@unife.it
3 Centro Interuniversitario per la Sismotettonica Tridimensionale, (CRUST), UR, 44122 Ferrara, Italy
4 Ermogenous 6, 41447 Larissa, Greece; abelesis1960@gmail.com (A.B.); giannistsentzos@gmail.com (I.T.)
* Correspondence: iannis@upatras.gr

Abstract: On 3 March 2021, a strong shallow earthquake affected northern Thessaly, Greece, with an epicenter close to Damasi village causing significant destruction of many stone houses. In this contribution, we provide fieldwork observations, satellite radar interferometry, mapping of the active faults exposed in the epicentral area, liquefactions and coseismic surface ruptures, and preliminary geomorphological analyses of the epicentral area. The geomorphological analysis is based on air photographs, digital surface models analysis, Real-Time Kinematik (RTK) measurements with Global Navigation Satellite System (GNSS) receivers, and data from UAV flight campaigns. Although the seismotectonic setting of the area is complex and there is an apparent mismatch between field and interferometric data, the results of our investigations suggest that at least three fault segments were reactivated by the major shocks of the March seismic sequence. These tectonic structureslikely represent the westward propagation of the Tyrnavos Graben, where newly formed and inherited low-angle faults interplay in a complex manner.

Keywords: Damasi earthquake; surface ruptures; liquefaction features; low-angle normal faults; Greece

check for updates

Citation: Koukouvelas, I.K.; Nikolakopoulos, K.G.; Kyriou, A.; Caputo, R.; Belesis, A.; Zygouri, V.; Verroios, S.; Apostolopoulos, D.; Tsentzos, I. The March 2021 Damasi Earthquake Sequence, Central Greece: Reactivation Evidence across the Westward Propagating Tyrnavos Graben. *Geosciences* **2021**, *11*, 328. https://doi.org/10.3390/geosciences11080328

Academic Editors: Deodato Tapete and Jesus Martinez-Frias

Received: 19 May 2021
Accepted: 29 July 2021
Published: 2 August 2021

Publisher's Note: MDPI stays neutral with regard to jurisdictional claims in published maps and institutional affiliations.

Copyright: © 2021 by the authors. Licensee MDPI, Basel, Switzerland. This article is an open access article distributed under the terms and conditions of the Creative Commons Attribution (CC BY) license (https://creativecommons.org/licenses/by/4.0/).

1. Introduction

The 2021 seismic sequence of Central Greece, called hereinafter the Damasi earthquake, began on the 3rd of March with an Mw 6.3 earthquake (magnitude from NOA). Its epicenter is located close to the village of Damasi. This earthquake caused the significant destruction of many stone houses in villages of the epicentral region, but fortunately, there were no casualties. A second earthquake (Mw 6.0) occurred on March 4th (magnitude from NOA) (Figure 1), while numerous aftershocks were recorded in the following days clustering progressively towards the NW, inducing further damage to buildings. The seismic cluster is tightly confined on the area of Damasi and Vlachogianni villages during the first 12 or more hours after the 3rd of March event and then after the 4th of March event expanded north-westwards for more than 25 km. In map view, the aftershocks form a 45 km-long and 18 km-wide zone, while their recorded depths range between ≈2 and 20 km, with the majority of them placed below 10 km (Figure 1c). Their focal mechanisms are compatible with the regional kinematic model indicating normal faulting. The cluster continues to show signs of activity for the interval of 4 months after the major March sequence (Figure 1c).

The seismically affected area we investigated represents a large sector of Northern Thessaly, characterized by lithologies belonging to the Pelagonian superterrane [1] and consisting of gneiss and schists Palaeozoic in age, Triassic recrystallized carbonates, and

post-Alpine sedimentary formations. The study area is crossed by the valley of the Titarissios River, which drains a large portion of the Antichasia Mountains and the western Olympus Mount [2,3]. In terms of geological evolution, the area was affected by Cretaceous accretionary orogenic stages and the reappraisal of convergence-contraction during the Palaeogene; it then entered a period of crustal extension since latest Miocene-Pliocene.

Because of the overall tectonic evolution, the present-day Thessalian geomorphology and orography are controlled by major normal faults [4–11]. These faults are grouped into two sets. NW-SE trending faults mainly developed during the Pliocene-Early Pleistocene NE-SW crustal stretching caused by the post-orogenic collapse [2,8]. A second one consisting of roughly E-W-to-ESE-WNW oriented structures that started forming from the Middle Pleistocene due to the effects of the slab roll-back affecting most of the Aegean Region i.e., [10] (Figure 1). However, these newly formed faults are either in a growing stage or are still interacting with, or cause reactivations of, inherited structures, including low-angle ones.

The regional hydrographic network and the fluvial geomorphology in the Thessaly area are strongly influenced or governed by active faults. Clear examples are the Pinios River east of Larissa [12] and the central reach of the Titarissios River, whose valley south of Damasi was completely abandoned sometimes during Late Quaternary when the river was captured and diverted eastwards towards the Larissa Plain. This phenomenon was a consequence of the progressive growth of the Tyrnavos and Larissa faults [13]. These tectonic structures are two north-dipping high-angle faults with normal kinematics. In particular, the well-exposed Tyrnavos Fault affects the Triassic crystalline limestone of the Pelagonian basement, but locally also Pliocene and Quaternary deposits [4]. The general trend is E-W, though it shows a slightly right-bending geometry. The well-defined fault trace was mapped in detail for more than 12 km [6]. Based on remote sensing techniques, it can be followed eastwards across the northern Larissa Plain with a possible maximum length of about 15 km. Towards the west, the surface evidence stops north of the Damasi village. Several palaeoseismological trenches documented its persistent recent activity [14,15].

In a right-stepping geometry and with a partial overlap, the synthetic Larissa Fault also shows evidence of neotectonic activity [16]. This structure borders to the south the Tyrnavos Graben, striking ESE–WNW for about 25 km [4] (Figure 1). The Late Quaternary evolution of the Pinios River and its alluvial plain was strongly influenced by the activity of this fault [12]. Nevertheless, due to (i) the coincidence of the riverbed with the fault sector crossing the Triassic limestone and (ii) the footwall block uplift and exposure of Late Pliocene and Pleistocene poorly consolidated deposits, the Larissa Fault is probably geologically less known among the major faults bordering the northern Thessaly basin. Whatever the case, archaeoseismological information suggests the occurrence of moderate-to-strong historical earthquakes reactivating this major tectonic structure [16,17].

Antithetic to the Larissa and Tyrnavos faults and bordering to the north the graben are the Gyrtoni and Rodia Faults [7,9,11,18]. For both faults, palaeoseismological investigations and morphotectonic analyses document the recent linear morphogenic activity [19], however, none of them reactivated during the March 2021 seismic sequence.

Notwithstanding the impressive seismotectonic evidence characterizing the major faults bordering the Tyrnavos Graben suggesting the occurrence of a seismic gap [7], the historical seismic record for the broader area is relatively poor (e.g., [20,21]), especially if compared to that of the southern Thessalian sector, where several moderate-to-strong events occurred in the 20th century (e.g., [22–25] and Table 1).

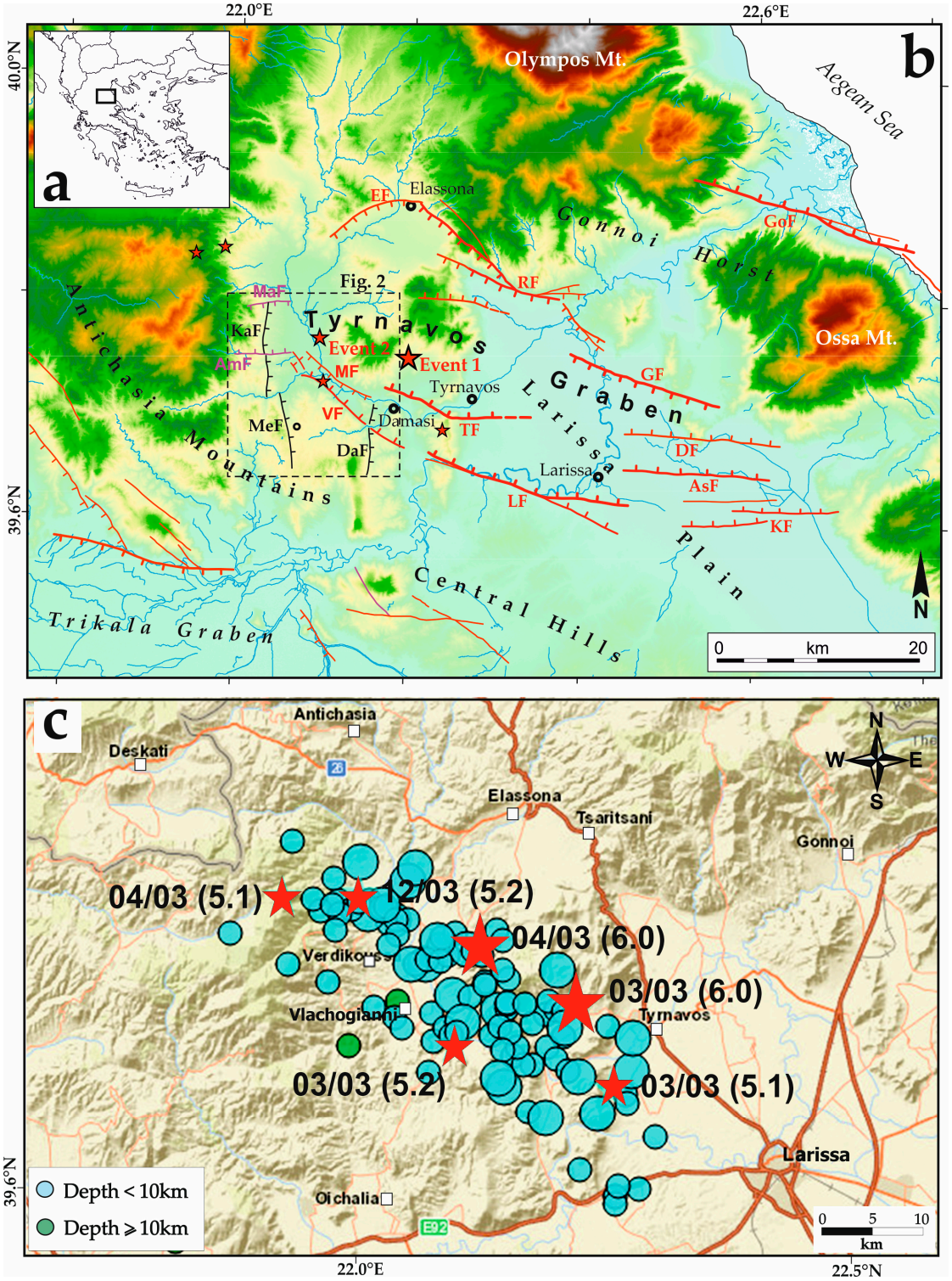

Figure 1. (**a**) Inset map of Greece showing the study area. (**b**) Tectonic map of the Tyrnavos Graben developed in northern Thessaly since Middle Pleistocene (modified from [4,7] and this study). (**c**) Simplified map showing seismic cluster with events >Mw 3.5 from 1 March 2021–15 July 2021 (data derived by https://bbnet.gein.noa.gr/HL/databases/database, accessed on 25 July 2021). Red stars in (**b**,**c**) indicate epicentres of major shocks (dimensions are proportional to magnitudes). Faults labels are as follows: EF: Elassona; RF: Rodia; GoF: Gonnoi; GF: Gyrtoni; MaF: Magoula; AmF: Ambelia; MeF: MegaloEleftherochori; MF: Mesochori; VF: Vlachogianni; TF: Tyrnavos; LF: Larissa; DF: Dimitra; AsF: Asmaki; KF: Kastri.

Table 1. Various sources of historic seismicity of Thessaly based on [21] and references therein. I_{max} = maximum macroseismic intensity; I_{TG} = maximum macroseismic intensity in Tyrnavos Graben; *TG* = Tyrnavos Graben, sector = location of epicentral area with respect to TG; I_{TG} = maximum intensity within TG (observed in group A and inferred in B–D); M_m = macroseismic magnitude.

Earthquakes	Date	M_m	I_{max}	Epicentre	Sector	I_{TG}
Instrumentally Recorded	13 May 1995	6.6	IX	Kozani	NW	IV–V
	9 July 1980	6.4	VIII	Almyros	S	IV–V
	8 March 1957	6.8	IX	Velestino	S	V(–VI)
	19 April 1955	6.2	VIII	Volos	S	V
	30 April 1954	6.7	IX	Sophades	SW	VI–VII
	1 March 1941	6.1	VII	Larissa	TG	(VIII–)VII
	31 March 1930	6.1	VIII	Pouri	SE	V
	23 February 1930	6.0	VIII	Keramidi	E	V
	22 October 1911	6.0	VIII	Keramidi	E	VI
Historical written sources	**Date**	M_m	I_{max}	**Epicentre**	**Sector$_{TG}$**	I_{TG}
	20 January 1905	6.2	X?	Skiti	E	VII
	17 November 1901	5.0?	VI–VII?	Verdikoussa	NW	?
	15 May 1900	5.0?	VI(–VII)	Sykourio	TG	VI(–VII)
	9 January 1892	5.0?	VI(–VII)	Larissa	TG	VI(–VII)
	3 October 1868	6.3	VIII	Skiathos Is.	SE	-
	21 October 1864	6.0	VII	Pelion	SE	-
	3 March 1837	?	VI–VII	Stomio	NE	?
	19 June 1787	6.0	VII	Meteora	W	?
	8 September 1781	6.0?	VII?	Larissa?	TG?	VII?
	16 March 1773	6.4	VIII	Almyros	S	?
	9 November 1766	6.3	VIII	Elassona	NW	?
	12 February 1743	6.6	VIII	Almyros	S	V
	1 September 1735	6.3	VII	Meteora?	W?	?
	1731	6.0	VII	Larissa	TG?	VII
	25 February 1674	?	?	Meteora	W	?
	26 January 1674	?	?	Meteora	W	?
	31 March 1661	6.2	?	Meteora	W	?
	6 March 1621	6.0	VI	Meteora	W	?
Archaeological evidences	**Date**	M_s	I_{max}	**Epicentre**	**Sector$_{TG}$**	I_{TG}
	7th–15th c. AD	6.0–6.5	VIII–IX	Larissa?	TG	VIII–IX
	2nd–1st c. BC	6.0–6.5	VIII–IX	Rodia	TG	VIII–IX
Palaeoseismological evidences	ca. 3 ka BP	6.4?	VIII–IX	Rodia	Rodia F.	VIII–IX
	6.9–5.3 ka BP (-Present)	6.0–6.5	VIII–IX	Tyrnavos	Tyrnavos F.	VIII–IX

The present contribution aims at describing the reactivation of the complex fault array that cross the Damasi earthquake epicentral area and the associated coseismic environmental effects of the sequence based on systematic field observations and satellite radar interferometry. Furthermore, considering the crustal scale Tyrnavos Graben, best studied east of the epicentral area of the Damasi earthquake sequence, we intend to provide new information on how the recent tectonic evolution of the Vlachogianni–Damasi region is correlated with the mapped Tyrnavos Graben. Indeed, we intend to provide new information on the recent tectonic evolution of the epicentral area. More seismological details are beyond the goals of this research, and we address the reader to more specific papers (e.g., [26,27]).The post event investigation includes mapping of the active faults exposed in the epicentral area, liquefaction features, and coseismic surface ruptures. We also present preliminary geomorphological analyses of the epicentral area, which are based on historical air photographs and digital surface model analysis for highlighting the most important active faults in the area. Real-Time Kinematik (RTK) measurements with Global Navigation Satellite System (GNSS) receivers and data from UAV flight campaigns (Figure 2) were used to precisely constrain the coseismic deformation across reactivated faults.

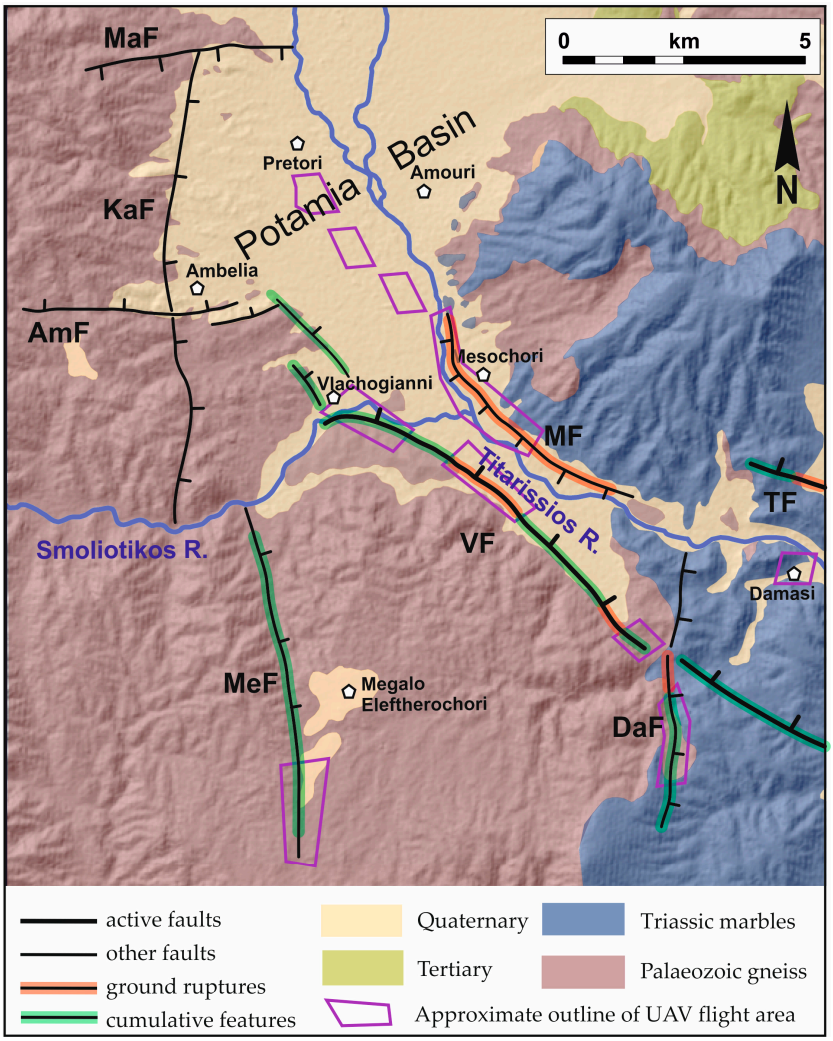

Figure 2. Geological map of epicentral area of Damasi earthquake showing main faults in epicentral area. Areas where detailed UAV field inspection took place are also shown.

2. Material and Methods

2.1. Mapping of Fault Array and Documentation of Ground Failures

During field inspection, numerous environmental effects of the 3rd and 4th March 2021 earthquakes were mapped at numerous sites in a broad area between Tyrnavos town, Damasi and Verdikousa villages, and Elassona town. These effects primarily include coseismic ground ruptures (Figure 2) and liquefaction failures (Figure 3). Our observations were collected through field mapping over the seismically affected area, which is clearly defined by the SAR differential interferometry, while repeated SAR scenes processing, from the Sentinel-1 satellite, for pre-and post earthquake periods, provided more key evidence since the seismic sequence included two strong earthquakes and a moderate one.

During the fieldwork, we focused on areas characterized by significant clustering of secondary effects, like liquefaction phenomena and/or ground failures, where accurate mapping by UAV photogrammetric flights was performed (Figure 2). Our flights followed the methodology developed by [28–30]. Our field surveys started on the morning of the 4th of March 2021 and lasted for almost three weeks. During the field campaign, we produced more than 30 orthophoto maps (300 m-long by 200 m-wide) recording the liquefaction features and the seismically induced surface ruptures. Concerning the latter, we recognized at least five fresh scarps associated with fracture opening, where we further conducted detailed morphological and structural analyses.

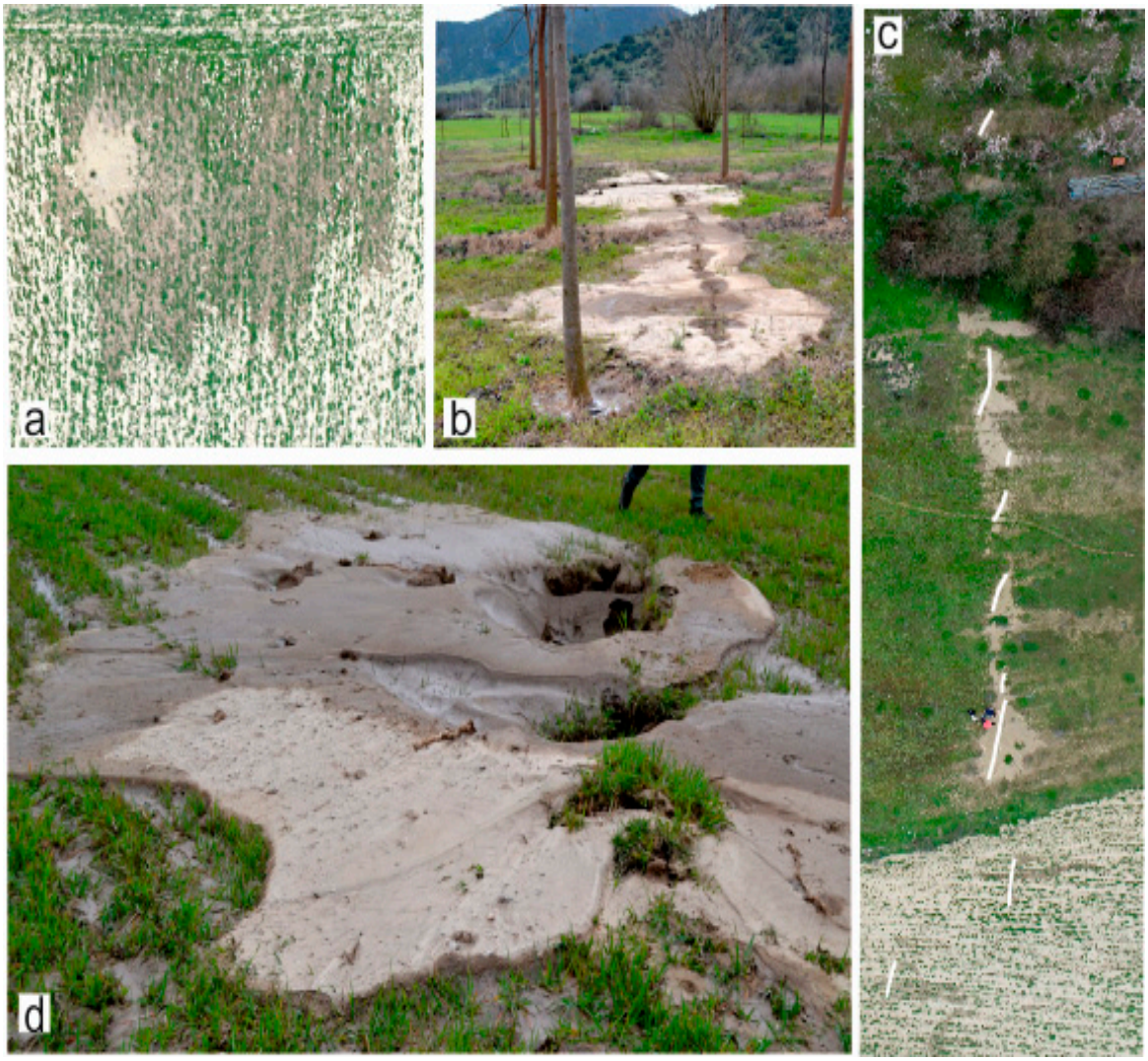

Figure 3. (**a**) Asymmetric sand blow with a single crater. Footage captured from a drone at a flight height of 80 m, width of photo 50 m. For this type of sand blow, local witnesses reported continuous water flow for at least 2-h after the M6.3 earthquake. (**b**) Field photograph of aligned and coalescent sand blows. Length of the series of blows is approximately 15 m. (**c**) Aerial view showing tens-of-meters long liquefaction features. These asymmetric sand blows developed parallel to Vlachogianni Fault. Note asymmetry of sand blows that is observed by water downslope movement and asymmetry in blow development. White lines emphasize the craters alignment. Overall length of observed feature is 75 m. (**d**) Multiple craters in a sand blow. Note dry sands in frontal part of picture and wet sands on back of photo. Pebbles in dry part of sand blow indicate their relationship with 3 March M6.3 Damasi earthquake, while wet material is related to 4 March 2021 M6.0 earthquake. Width of sand blow is about 5 m.

2.2. Liquefaction Features

Among the secondary effects associated with the major shocks of the seismic sequence, the most prominent ones are probably represented by diffuse liquefaction phenomena. The associated liquefaction features mainly affected two areas: the first and the most important is along the Titarissios Valley, being a few kilometers away from the epicenter, and a second one close to the Piniada Valley, representing a reach of the Pinios River at a distance of more than 18 km south of the mainshock epicenter. In the current contribution, we will focus on the Titarissios Valley since its observed features are correlated with primary earthquake evidence. In particular, many sand blows with maximum diameters up to 30 m (Figure 3a) and generally in the order of 10 m were observed within the epicentral area. The associated craters formed by the dewatering and sand ejection from the shallow subsoil are typically 0.3–0.5 m in diameter. The thickness of the sand volcano deposits was higher around

the crater and gradually decreased radially, with a varied range of a few cm up to 50 cm. Sand volcanoes could be divided into symmetrical and asymmetric types. The formers are concentrated on flat areas, while the latter in areas with topographic irregularities (Figure 3b–d, respectively). The sand blows occurred either as isolate features or clusters (Figure 3a–d, respectively). Aligned volcanoes generally had a prevailing NW orientation, with some liquefaction craters showing NE-distribution direction.

Overall, two main types of liquefaction features were observed in the area between Pretori and Damasi villages, with most of them concentrated between Vlachogianni and Mesochori villages. Finally, sand blows consisted of different sand types, e.g., coarse dry at the lower part and wet fine on top (Figure 3d). Our detailed observations in these 'double' liquefaction deposits suggest that sand ejection was caused by both the mainshock (3 March 2021) and the largest aftershock (4 March 2021). Secondly, collapsed structures were mapped to be associated with dikes, where soft-sediment faults are intruded by dikes. This second type of structure seems to form close to the Titarissios riverbank and associate with lateral spreading or collapse due to consolidation or mobilization of an underlying liquefiable sand level(s).

2.3. SAR Interferometry of the Epicentral Area

SAR interferometry was established as a valuable technique for Earth deformation monitoring caused by earthquakes since 1992, when radar satellite data acquired by ERS-1 were successfully used to map the Landers earthquake in California, USA [31]. The aforementioned SAR interferometry was an inspiration to several scientists studying ground deformation caused by earthquakes using Synthetic Aperture Radar (SAR) satellite missions [32–37]. Over the years, new SAR satellite missions were launched to contribute to more detailed analyses and a better understanding of earthquake deformation. Sentinel-1 satellite constellation, developed by European Space Agency (ESA), opened up new possibilities through the increased number of observations, the systematic global acquisitions, the short revisit times, and the more stable orbits [37]. In that context, Sentinel-1 data are ideal for the postseismic deformation mapping, resulting from the occurrence of earthquakes on 3 March, 4 March, and 12 March, 2021. In the present study, data obtained from SLC Sentinel-1, ascending and descending orbits, were processed using Sentinel Application Platform (SNAP) developed by Brockmann Consult, SkyWatch, and C-S. The characteristics of the interferometric pairs are displayed in Table 2.

Independently from other research groups (e.g., [38]), we also analyzed SAR interferograms with the aim of better understanding the coseismic surface deformation. The results of our differential interferometric analyses are represented in Figure 4. In particular, the first Sentinel-1 ascending interferogram was created by images spanning the first seismic event between 25 February and 3 March, 2021 (Figure 4a). Fringes are very dense, and a local linear loss of coherence is identified on an axis starting from the center of the interferogram and extending to the northwest. The second interferogram, generated by the Sentinel-1 images of 3 and 9 March 2021, contributed to the measurement of coseismic deformation produced by the 4 March event (Figure 4b). Interferometric fringes moved to the northwest, while a similar linear loss of coherence is detected. Unfortunately, the isolation of the coseismic deformation for the second event was only possible through ascending data processing. Besides, two additional Sentinel-1 interferograms were created to capture the deformation that occurred by both major events. The ascending and descending interferograms are in Figure 4c,d, respectively, where two areas of maximum deformation could be clearly observed. The deformation mapping of the third major shock (12 March) reveals the generation of another area of subsidence further northwest (Figure 4e,f). Overall, the quality of Sentinel-1 interferograms is remarkable, exhibiting ultrahigh coherence and low tropospheric disturbances. Concerning InSAR processing, we removed the topographic component using a Shuttle Radar Topography Mission (SRTM) 1 Arc-Second Global DEM, while phase filtering was implemented through an adaptive algorithm proposed by [39].

Table 2. Details of InSAR processing using Sentinel-1 data.

Interferometric Pairs		Pass	Track	Bperp (m)	Btemp (Days)	Modeled Coherence
25 February 2021	3 March 2021	Ascending	102	43.81	6	0.96
3 March 2021	9 March 2021	Ascending	102	28.39	6	0.97
25 February 2021	9 March 2021	Ascending	102	15.54	12	0.97
25 February 2021	15 March 2021	Ascending	102	13.78	18	0.97
2 March 2021	8 March 2021	Descending	80	52.03	6	0.95
2 March 2021	14 March 2021	Descending	80	53.01	18	0.94

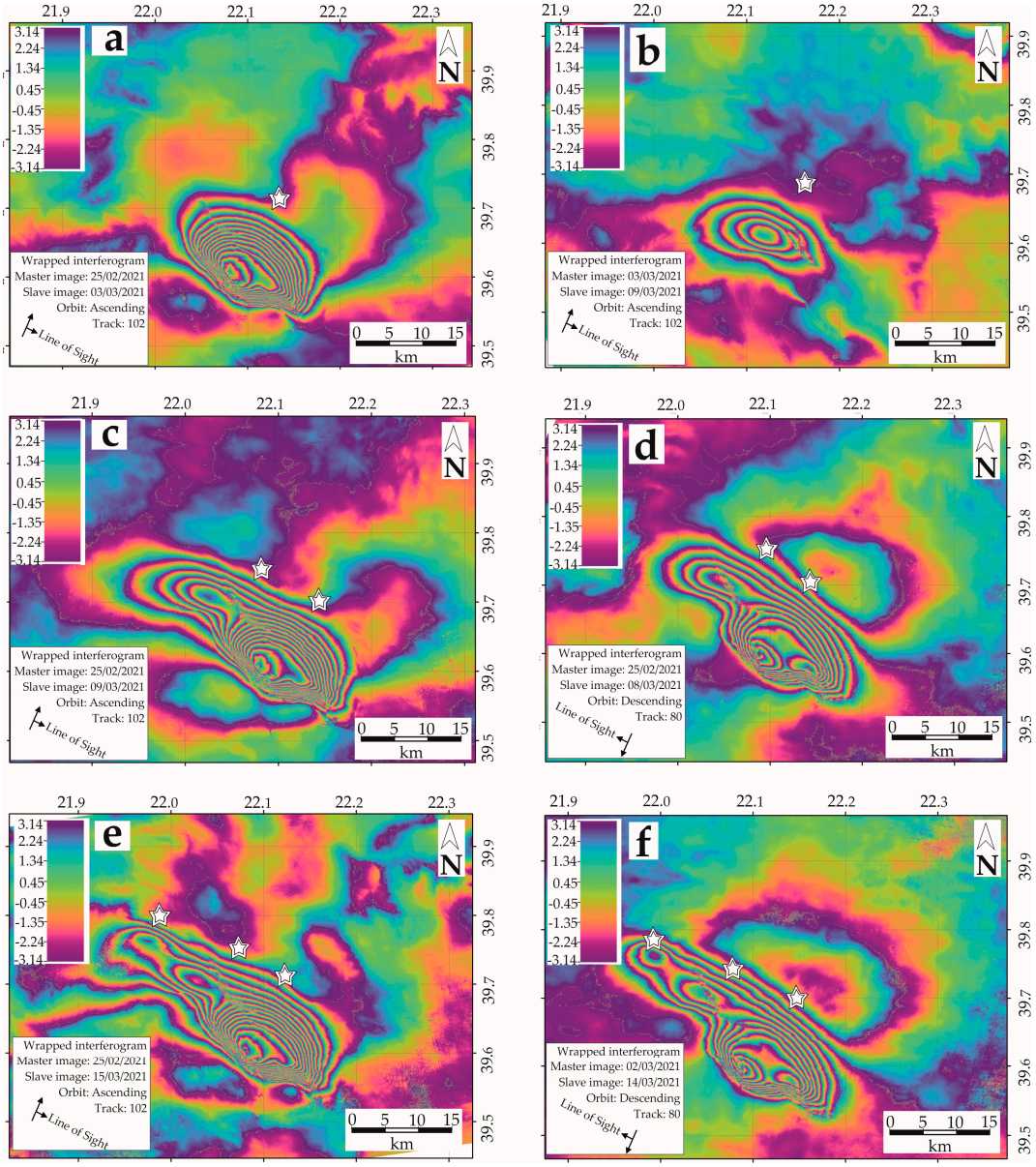

Figure 4. Sentinel-1 interferograms. (**a**) Sentinel-1 ascending interferogram capturing deformation of 3 March earthquake. (**b**) Sentinel-1 ascending interferogram capturing deformation of the 4 Marchearthquake. (**c**) Sentinel-1 ascending interferogram capturing deformation of 3 and 4 March earthquakes. (**d**) Sentinel-1 descending interferogram capturing deformation of 3 and 4 March earthquakes. (**e**) Sentinel-1 ascending interferogram capturing deformation of 3, 4, and 12 March earthquakes. (**f**) Sentinel-1 descending interferogram capturing deformation of 3, 4, and 12 March earthquakes.

3. Coseismic and Cumulative Faulting Evidence

Overall, field data and the interferograms show that the causative faults of the Damasi seismic sequence occupy the westernmost sector of the Tyrnavos Graben [7] (Figure 1) and probably represent the embryonic stage of the lateral propagation of the northern Thessalian basin. Indeed, these seismogenic structures were not on geological maps and/or their tectonic features were not classified as active due to poor morphological expression or ambiguous seismotectonic evidence. After the mainshock of the 3rd of March and the major aftershock of the 4th of March, we focused our field investigation on the Tyrnavos (TF), Vlachogianni (VF), and Mesochori (MF) faults, as well as on other tectonic structures that possibly played a role in the distribution of the coseismic deformation (Megalo Eleftherochori, MeF, Damasouli, DaF, Kalivia, KaF, faults; Figure 2). Fieldwork and morphotectonic analyses were devoted to recognizing possible reactivations and the role of these structures during the March 2021 seismic sequence, when this work was completed, although the seismicity remained active during April, May, and June 2021.The trace of all these faults locates within the InSAR fringes, which locally show some disturbances.

Based on the preliminary epicentral location of the mainshock (Figure 1), the first candidate as the causative fault was considered the WNW-ESE trending Tyrnavos Fault, which was thus promptly surveyed. However, except for minor surface ruptures associated with few millimeters of opening across two asphalted roads crossing N-S the valley north of the Damasi village (Figure 2), no further evidence was observed. In the meantime, the first DInSAR results confirmed the lack of significant displacement along the trace of and associated with the Tyrnavos Fault [38].

As concerns the NW-SE oriented tectonic structures affecting the epicentral area, the Vlachogianni Fault is certainly the most prominent (Figures 2–4). Although it is segmented at the surface, it has a possible total length of ca. 15 km. The northwest sector seems to split into a couple of branches and progressively loses any surface expression within the Quaternary alluvial plain sediments flooring the Potamia Basin.

The clearest evidence of recent activity was observed along the central sector of the VF, where the fault borders to the south an 8–9 km-long reach of the Titarissios Valley (Figure 5). Here, the systematic post-event fieldwork supported by a UAV survey (Figure 6) allowed us to document the occurrence of several surface ruptures associated with the 3 March event. The mapped cracks show vertical offsets up to 10 cm and a maximum opening of about 4 cm. The rupture could be followed for at least 1 km across farmed fields, progressively disappearing in loose Quaternary deposits or grasslands. From the DSM of the area derived from the UAV flights data, it was also possible to reconstruct several topographic profiles across the morphological feature emphasizing the presence of ca. 1 m-high cumulative scarp affecting the Late Pleistocene alluvial cones (Figures 7 and 8). Since no liquefaction or lateral spreading phenomena were associated with the ground rupture and considering the presence of a clear flexural scarp, we tentatively suggest that the observed surface features are somehow linked to, and representative of, the coseismic reactivation of a fault at depth during the Damasi earthquake.

The fresh ground ruptures run at the base of, and parallel to, a linear cumulative scarp where a series of triangular facets are well-exposed (Figure 5) and document a long-lasting activity of these structures.

Towards the southeast, the VF crosses the Palaeozoic gneiss, where a 5 m-thick cataclastic zone was observed, documenting a superposed brittle behavior, possibly suggesting recent shallow reactivations. In this sector, fresh surface ruptures were also recognized at two locations associated with an array of open joints and small-scale rockfalls.

Figure 5. View of straight mountain front with faceted spurs that demarcates VF trace. Photo is taken from Bara Damasiou, looking west towards Vlachogianni village (Vv). Note series of facets exposed on footwall of fault. White arrow shows area where a sheep shepherd reported luminous aerial phenomena and waves on ground surface.

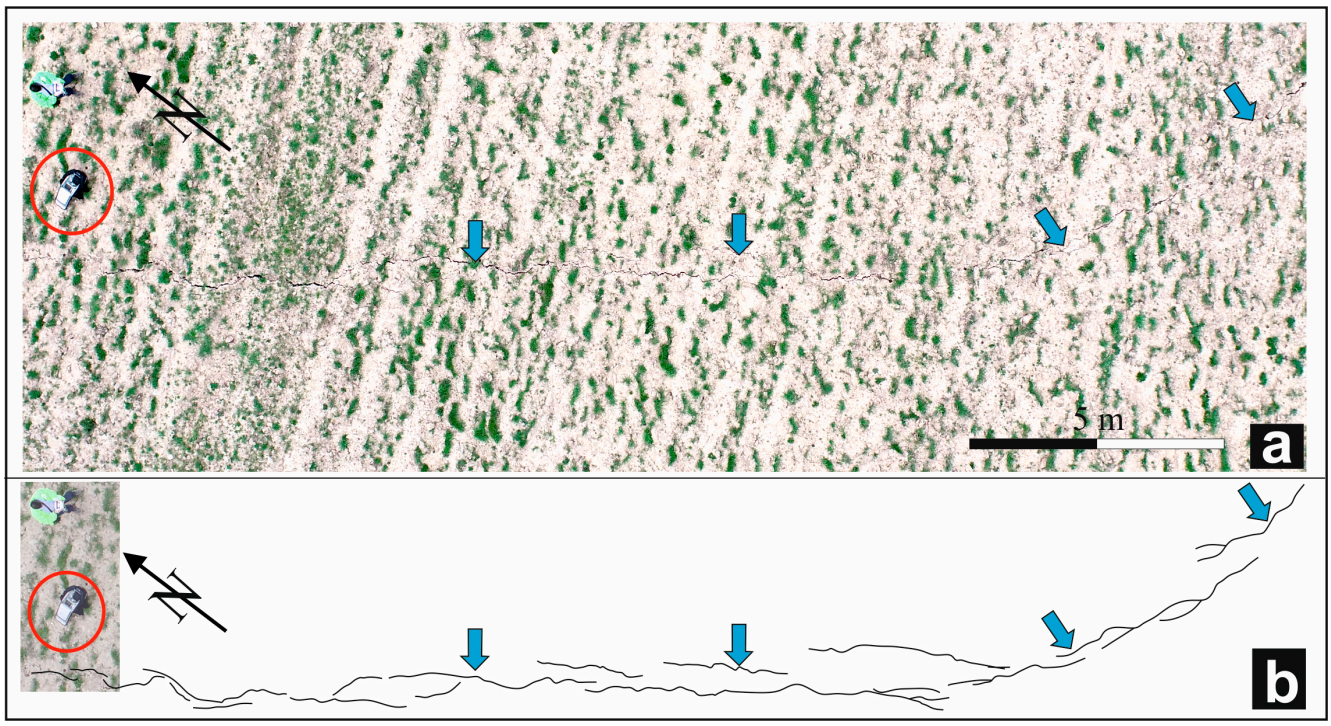

Figure 6. Drone capture of coseismic surface trace (**a**), as mapped on 4 March and its outline (**b**). This crack shows a maximum verticaloffset of 10 cm, and its surface trace is parallel with VF. Total trace of mapped rupture is ca. 1 km. Drone back-pack (in the red circle, 80-cm-long by 40-cm-wide) is used for scale.

At one of these locations, a local place called Bara Damasiou (Figure 2), sheep shepherd Vlioras Panagiotis observed luminous aerial phenomena that appeared at a distance of less than 100 m from the VF during the main earthquake event. Similar witnesses were recorded by our team relative to waves temporarily affecting the ground surface.

The Vlachogianni Fault was also mapped eastwards across the carbonate bedrock south of Damasi [7], where it loses any surface expression in correspondence with the N-S trending abandoned reach of the Titarissios Valley [13].

In the seismotectonic framework of the broader area, the trace of the VF is aligned with the active Larissa Fault well mapped on the other side of the valley [16]. The latter structure represents one of the major tectonic features of the whole Tyrnavos Graben [8,17] (Figure 1).

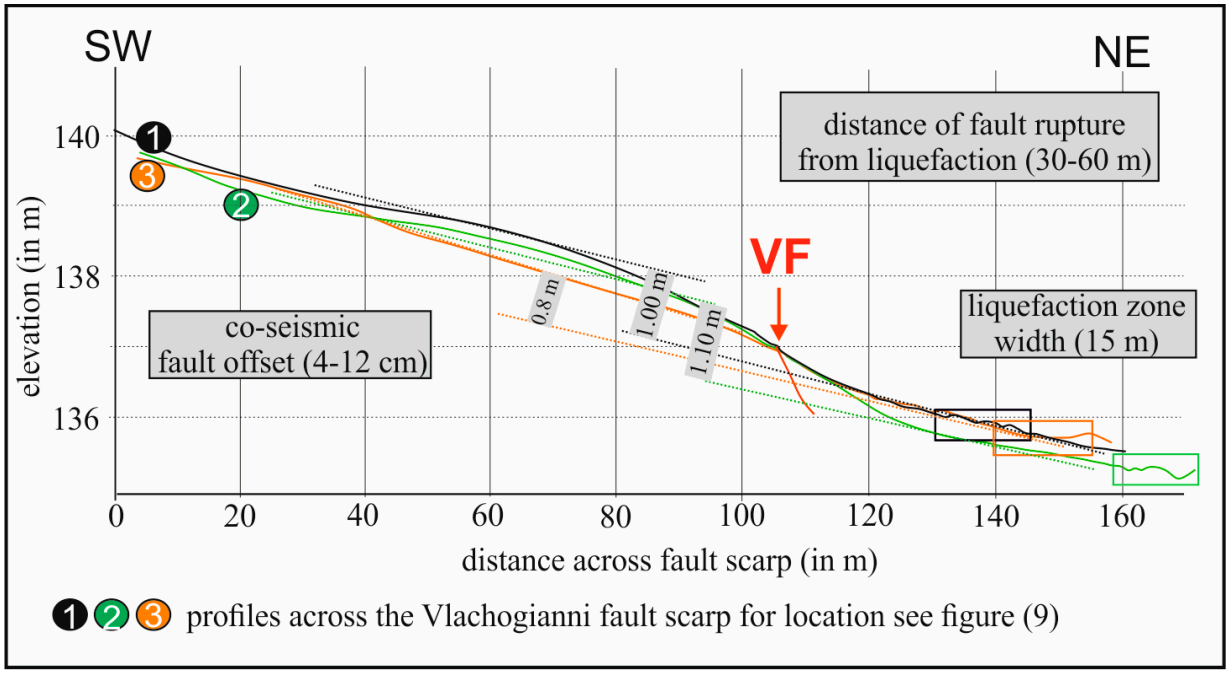

Figure 7. Fault scarp profiles across the VF coseismic ruptures (red arrow). For location of profiles, see the orthophoto map in Figure 8.

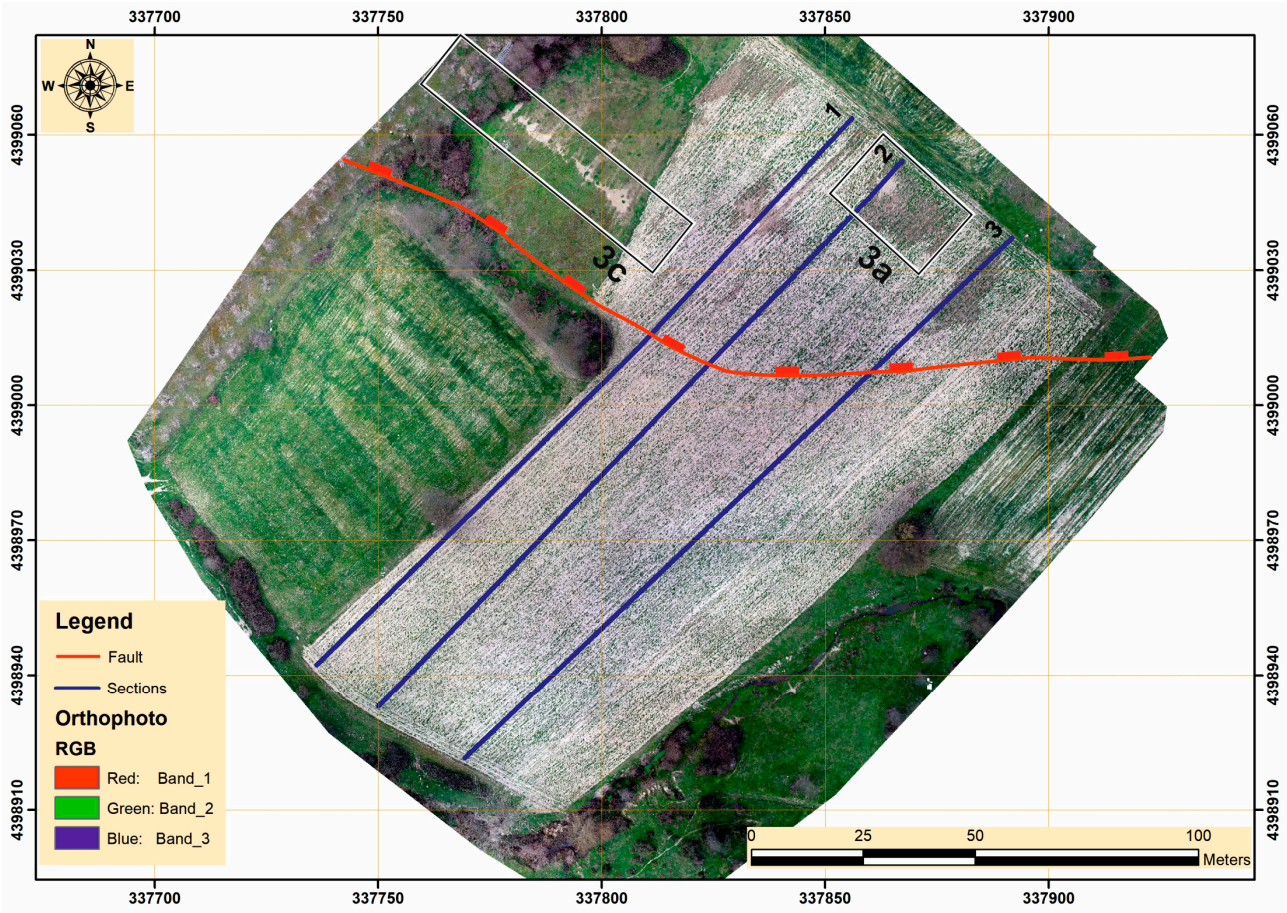

Figure 8. Orthomosaic showing location of three topographic profiles represented in Figure 7. Red line shows the co-seismic rupture.

Although the real cumulative displacement of the Vlachogianni Fault is difficult to estimate, a simple topographic analysis tentatively suggests a minimum value of 270 m. From borehole data drilled in the Potamia Basin (Figure 2), the thickness of the Pliocene-Quaternary sediment is about 180 m [40]. Accordingly, the cumulative displacement of the VF is possibly as much as 450 m. This total displacement is likely the result of two deformational phases: the Pliocene–Early Pleistocene and the Late Pleistocene–Present. However, the amount of displacement associated to the two extensional phases and their proportion are unknown.

Probably the most important surface rupture in terms of lateral continuity and amount of throw and opening was mapped along the northern side of the Titarissios Valley. On this side of the river, fresh ruptures were mapped, with a cumulative length of ca. 5 km. The observed displacement vectors document a south-dipping fault plane with normal kinematics. Throw values across this rupture are up to 28 cm, and openings are up to 10 cm (Figure 9). We refer to this newly formed and mapped structure as the Mesochori Fault (MF). Since these surface ruptures are close to the Mesochori village more than five oral witnesses confirm the correlation of this surface feature with the 3 March mainshock.

Figure 9. (**a**) A 3D overview of coseismic rupture along MF. Blue arrows show rupture trace represented in (**b**,**c**) along flexural fault scarp. Photo (**b**) is taken looking west, and surface offset is 28 cm. In this area, we excavated the palaeoseismological trench MeTr1. Photo (**c**) is taken looking east and shows MF flexural scarp with major and secondary coseismic ruptures.

The flexural surface scarp was also mapped through a systematic UAV flight campaign focusing on the sector with the best-preserved scarp (Figure 10a), where we excavated two palaeoseismological trenches, whose results will be presented in a separate paper. Based

on the UAV flight campaign, we prepared several detailed topographic profiles to better investigate the distribution of the surface displacement; for simplicity, we present in this work only eight of them. Examples are shown in Figure 10b, suggesting a cumulative scarp height in the order of 0.9 m.

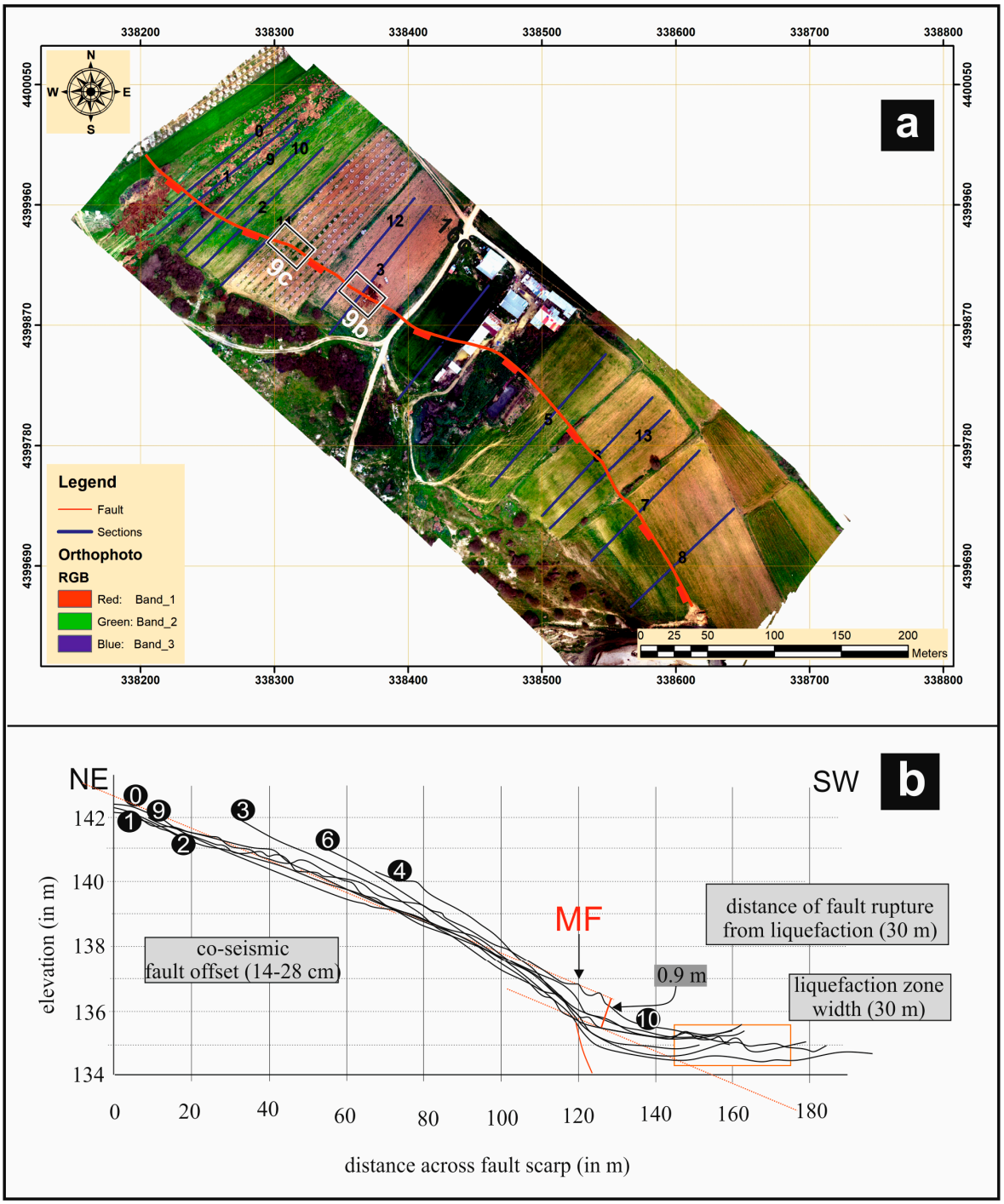

Figure 10. (**a**) Orthomosaic showing location of 13 profiles across the Mesochori (MF) scarp. Red line shows coseismic rupture. (**b**) Fault scarp topographic profiles across MF rupture.

Considering its parallelism and its proximity (less than 2 km) with the Vlachogianni Fault and its antithetic behavior, the MF represents a secondary tectonic structure, likely with an accommodation role relative to the north-dipping VF.

Northwest of the Vlachogianni Fault tip, the E-W trending Ambelia Fault together with the antithetic Magoula Fault (AmF and MaF in Figure 2, respectively) were tentatively suggested as possibly active [7]. However, no field evidence of coseismic reactivation was observed during our post event survey.

In contrast, we posed attention to some N-S oriented faults affecting the area, which undoubtedly represent inherited structures within the Pelagonian basement [41] but possibly played (and could continue to play) a role in the evolution of the Tyrnavos Graben.

The Megalo Eleftherochori Fault, MeF, runs W of the homonymous village and is characterized by a brittle-ductile shear zone (Figures 2 and 11a). This shear zone was likely active during the late Alpine stages [41] (i.e., Eocene–Miocene; for N-S trending faults by the Verdikousa village). The MeF includes a well-developed, 5-m-thick cataclastic zone with hematite concentration in a meter-thick fault core. The cataclastic zone suggests post-Alpine tectonic activity, and it was mapped along the bottom of a stream that runs parallel to the fault zone and drains into the Smoliotikos River (Figure 2). The stream is narrow in the south and gets wide in the north, probably in a relationship with the fluvial geomorphology and river developed along the fault. MeF is characterized by an east-facing scarp dipping less than 40° juxtaposing the Hercynian Pieria Granitoid Complex. The fault scarp becomes progressively smoother northwards, losing its prominent geomorphic expression in correspondence with the Smoliotikos River. It has a possible cumulative throw in the order of 150 m.

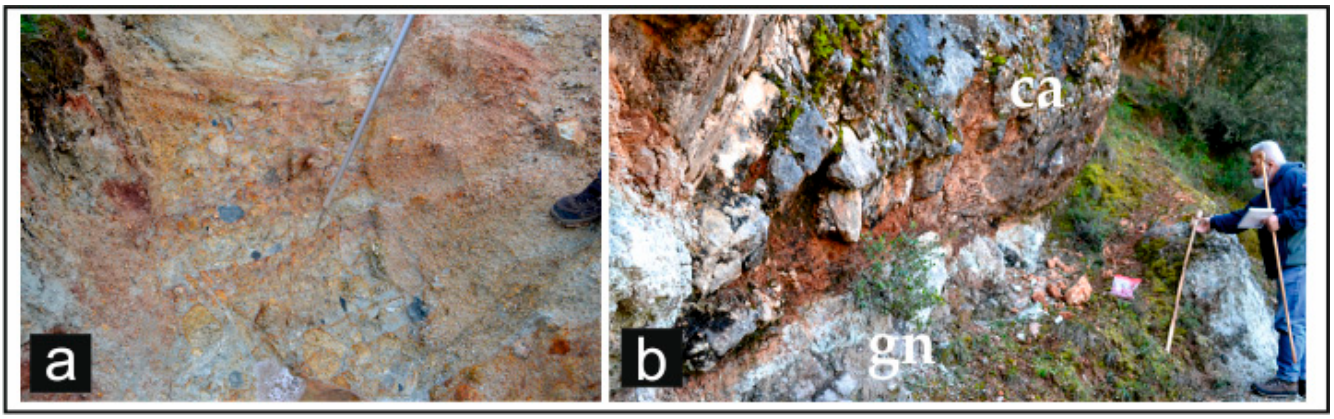

Figure 11. Key outcrops of two most prominent N-S trending faults in the epicentral area. (**a**) Cataclastic zone of MeF south of homonymous village. Photo is taken looking SE, and width of photo is approximately 1.5 m. (**b**) Cataclastic zone developed in DF including 1.5 m thick reddish to white rocks in central part of photo. Reddish rocks represent cataclasis in calcareous rocks, and whitish rocks represent gneissic cataclasites. Carbonate rocks are exposed in the DF hanging-wall block (ca) and gneisses (gn) in its footwall block. Photo is taken looking south.

North of the Smoliotikos River is the Kalivia Fault, KaF, which borders the Potamia Basin to the west (Figure 2). The KaF scarp is characterized by mountain front sinuosity index > 3, and thus, it could be considered as an eroded, probably inactive, fault. It is composed of minor segments and has a total throw in the order of 50 m. The south tip of the KaF is near its intersection with the Smoliotikos River, while the northern fault tip is difficult to recognize since it probably underlies post-Alpine sediments of the PotamiaBasin.

During the fieldwork, we also investigated the east-dipping Damasouli Fault (DaF; Figures 11b, 12 and 13). Although the trace of the fault north of the Vlachogianni Fault has relatively poor morphological expression, its southern part is instead well-marked for at least 2 km. In this sector, the fault is characterized by a cataclastic zone (Figure 12), where the fault rocks bear dip-slip kinematic indicators (Figure 13) documenting the uplift of the Palaeozoic schist-gneiss (hanging-wall) relative to the Triassic marbles (footwall). These kinematic data show clear evidence of inversion tectonics since this contact was originally a reverse fault [2,8].

Along with the well-exposed DaF, a series of small-scale landslides were recognized (Figure 12), and their density is about six landslides per square kilometer. At least two of these gravitational phenomena were triggered by the seismic sequence (Figure 12b,c), while open cracks and diffuse block toppling also developed (Figure 13).

Tectonic geomorphology provides a unique opportunity to investigate, through the analysis of landforms, the signature of the tectonic processes on landscapes over a period spanning the late Holocene to early Pleistocene, or even late Pliocene. Accordingly, we apply facets analysis and mountain front and river sinuosity patterns to infer the occurrence of intermediate- and long-term deformation in the study area.

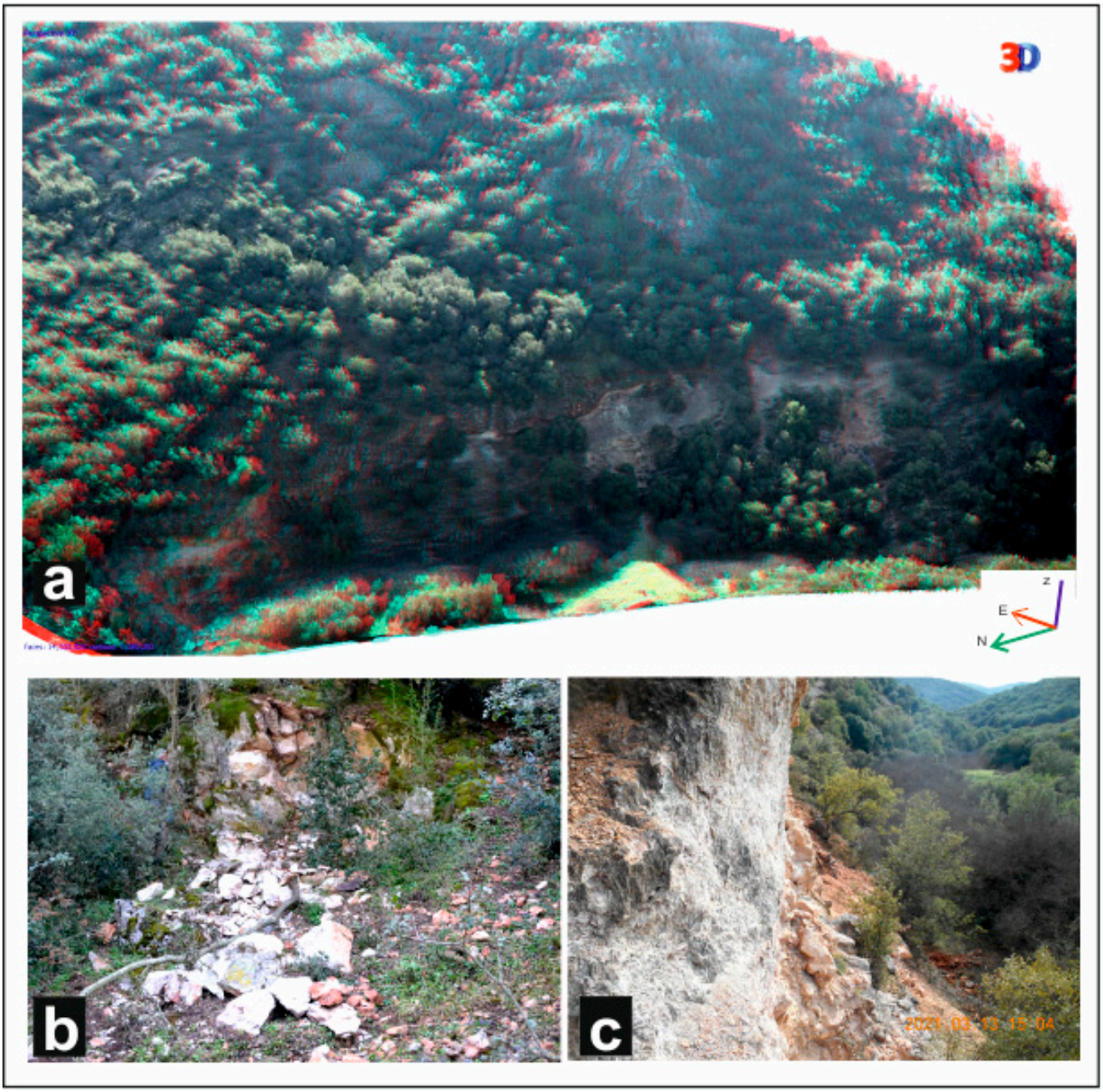

Figure 12. (**a**) Oblique 3D panoramic view of DaF and details of coseismically developed rockfalls. Model is based on drone captures looking east along the N-S trending valley. In valley bottom, Pelagonian gneisses are exposed. (**b**) Field photo showing a series of fallen blocks and freshly broken tree branches across trace of the DaF. Photo is taken looking east; length of rock fall is 15 m. (**c**) Rock fall across trace of the DaF. Photo is taken looking south. Width of photo is 20 m.

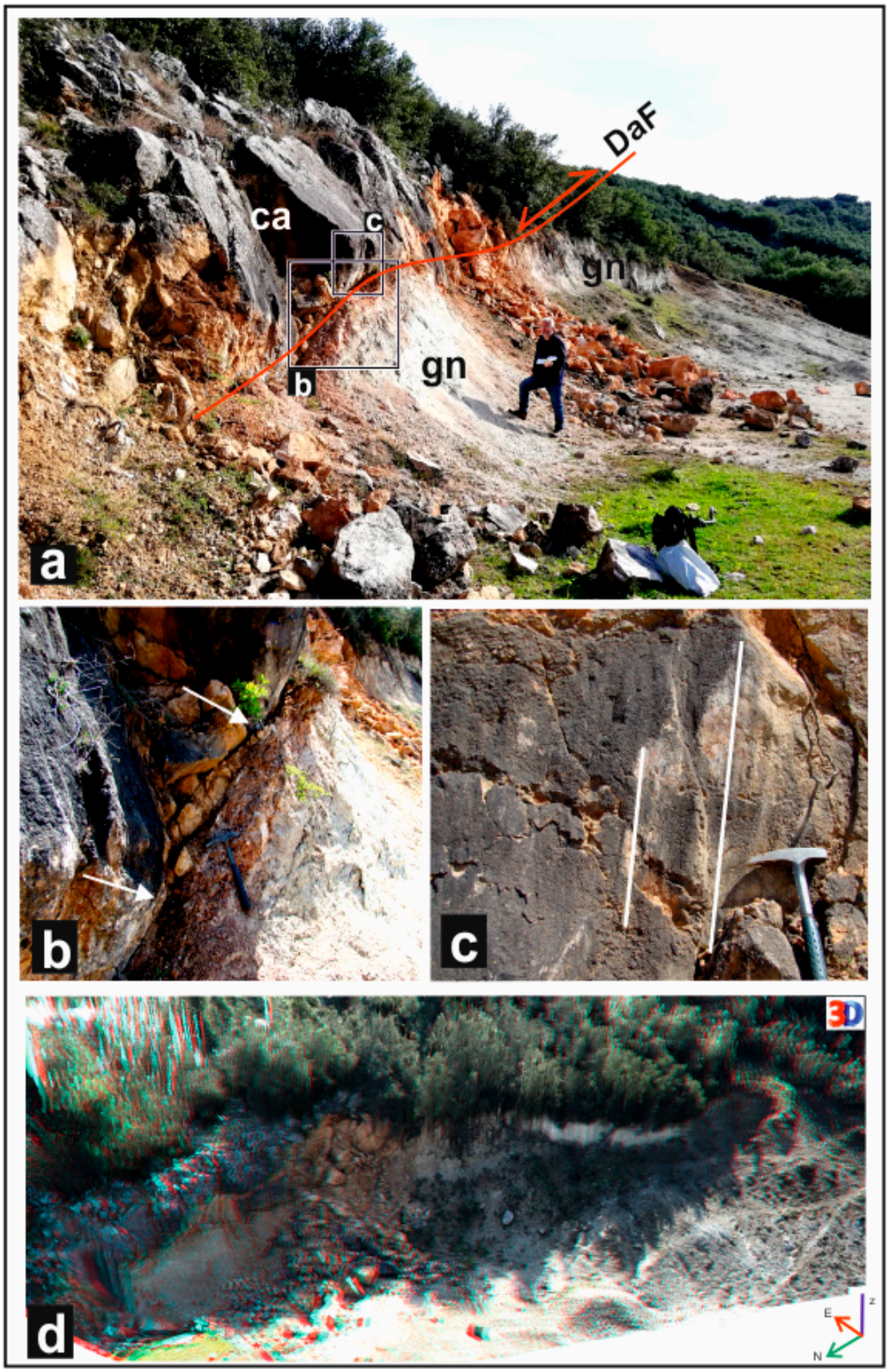

Figure 13. (**a**) View of DaF showing rockslides related with the fault outcrop and the two fault blocks. Photo is taken looking southeast. (**b**) Detail of rockslides developed during Damasi earthquake. Note that sliding site is crossed by a dense array of open cracks, most of which are trending NW. (**c**) Dip-slip slickenlines on carbonates along DaF zone. (**d**) Oblique 3D panoramic view of DaF and details of seismically induced rockfalls. Model is based on drone captures looking northeast.

Google Earth imageries used to determine the presence of morphotectonic features along the faults, like remarkable topographic breaks or steps (Figure 14). In this regard, both VF and MeF produce prominent fault scarps where morphometric analyses can be applied. For example, to evaluate the dissection of the mountain front, we estimated the Pf index for both faults.

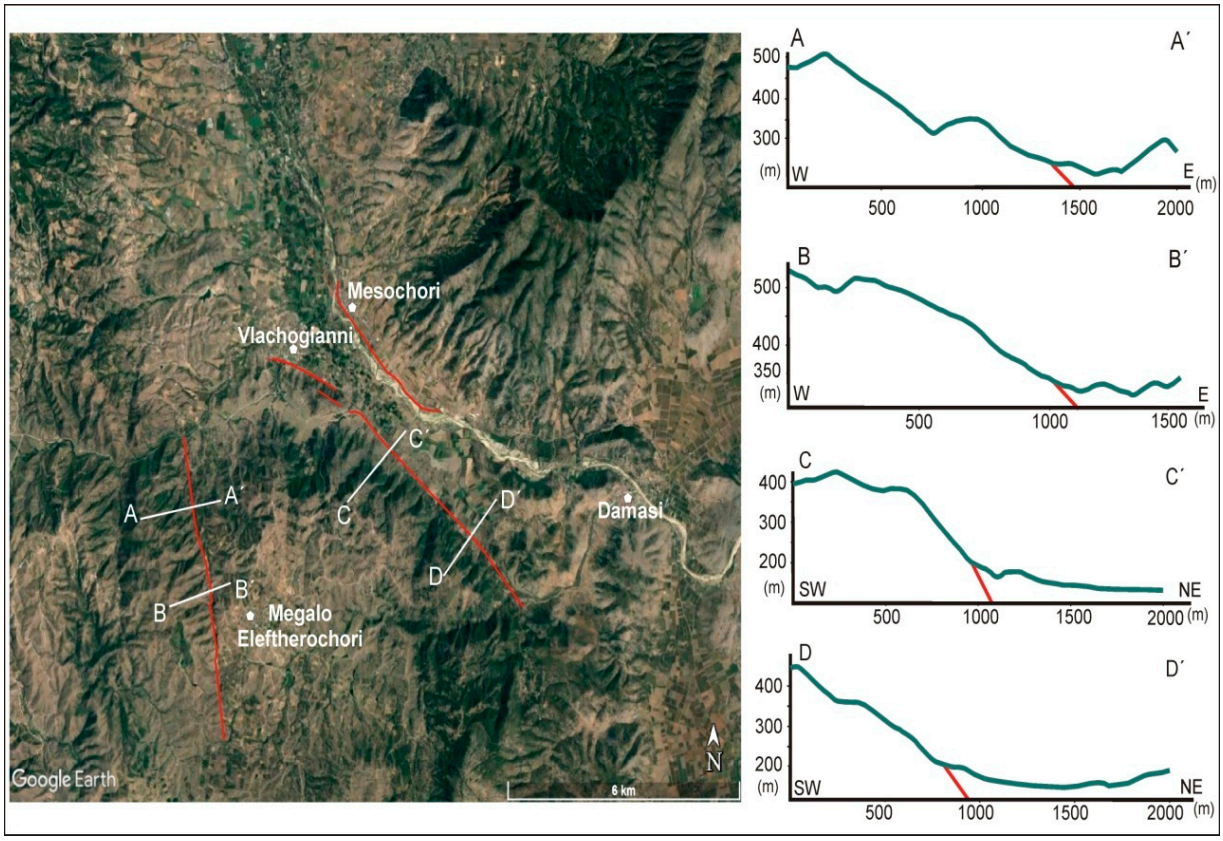

Figure 14. Sections along MeF (AA′ and BB′) and VF (CC′ and DD′) mountain fronts.

Mountain front facets on the MeF are primarily triangular. Steeper and wider facets are found in the central part of the fault, where different generations are observed, while their height decreases towards the south. The triangular facets are plotted from 1974 air photos printed at a scale of 1:18,000. The Pf index calculated from these images reaches 78% (Figure 15).

Also, along the VF mountain front, triangular facets are present occasionally in the northwest, as clearly observed on 1960 air photos (1:15,000 scale). The steepest facets are found along the central part in correspondence of the ground ruptures formed due to the March event. The Pf index for the VF is 87% (Figure 15). Triangular shaped facets, which generally form by erosion of fault-bounded mountain ranges, are arguably one of the most prominent geomorphic features on active normal fault scarps [18,42]. This evidence indicates that the VF had a recent (Late Quaternary) activity, likely characterized by distinct tectonic pulses as suggested by the higher (and older) triangular facets.

Concerning the MeF, though it shows some faceted spurs, its degree of recent activity is questionable. Similarly, the erosion across Kalivia Fault trace is prominent, and the overall tectonic geomorphology across the western border of the Potamia Basin suggest these are likely inactive structures.

No triangular facets were observed in the footwall of the Mesochori Fault, nor was a marked bedrock scarp. The lack of such geomorphic evidence and of detailed morphotectonic investigations (Figure 10) is likely the primary reason this faultwas never mapped before the Damasi earthquake sequence.

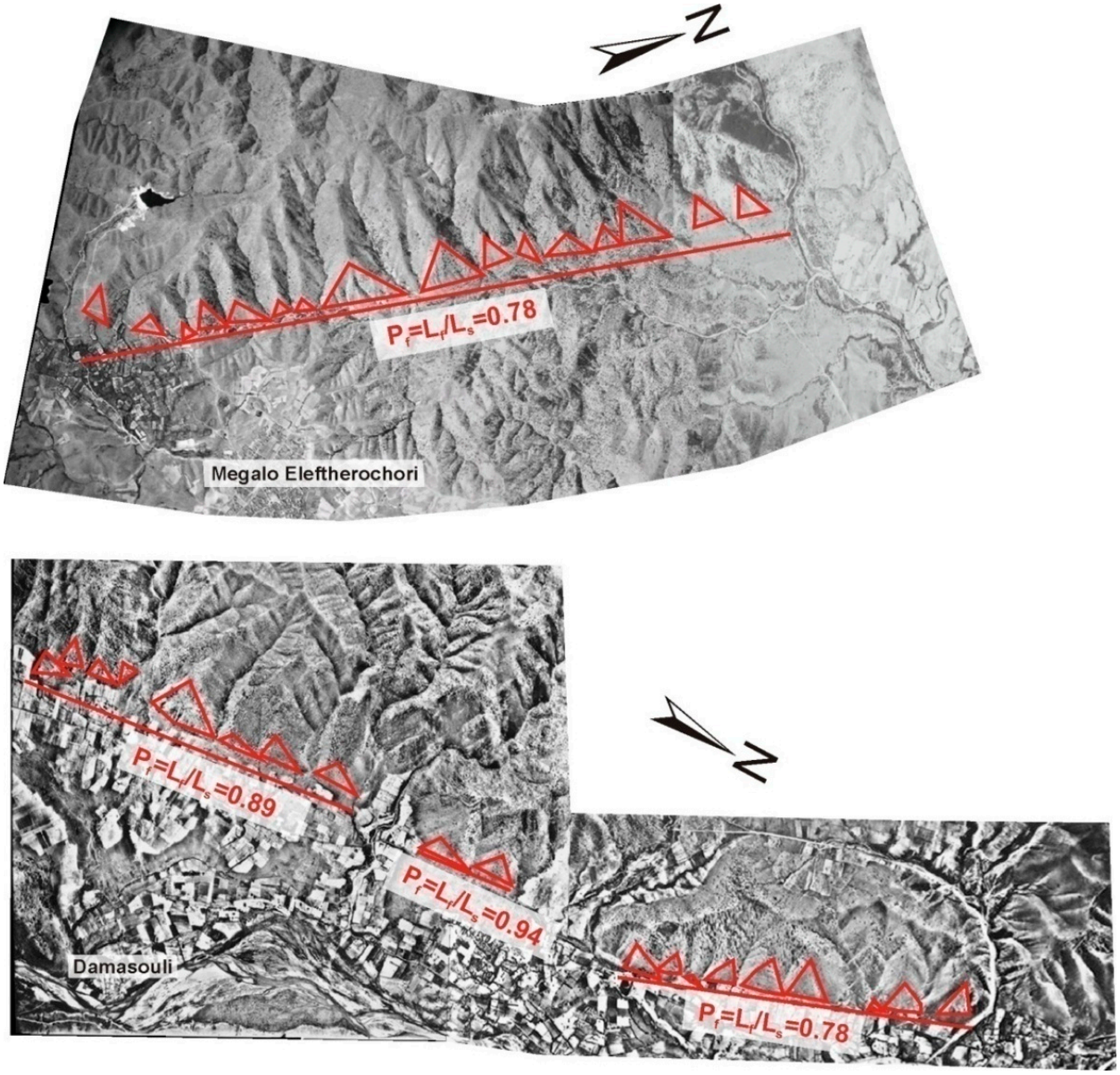

Figure 15. Triangular facets along mountain front of MEF (**top** figure) and along the VF (**down** figure). Triangular facets are plotted on 1974 (**top**) and 1960 (**down**) airphotos of G.Y.S.

It was recently proposed that the Late Quaternary regional hydrography was strongly influenced by the Vlachogianni, Larissa, and Tyrnavos faults (Figure 1). Although with different roles, all these tectonic structures contributed to the diversion of the Titarissios River (from its original southwards flow across the Piniada Valley to its final destination, the Karditsa basin) towards the Larissa Plain [12]. Notwithstanding, the secondary role of the Mesochori Fault certainly contributed to the structural control by laterally constraining a ca. 10 km-long reach of the Titarissios River. Along this valley, the river sinuosity has changed from 1945 to 2019 by increasing from 1.23 to 1.32 (Figure 16); this could reflect a possible change in sediment supply or some possible tilting of the valley floor [43].

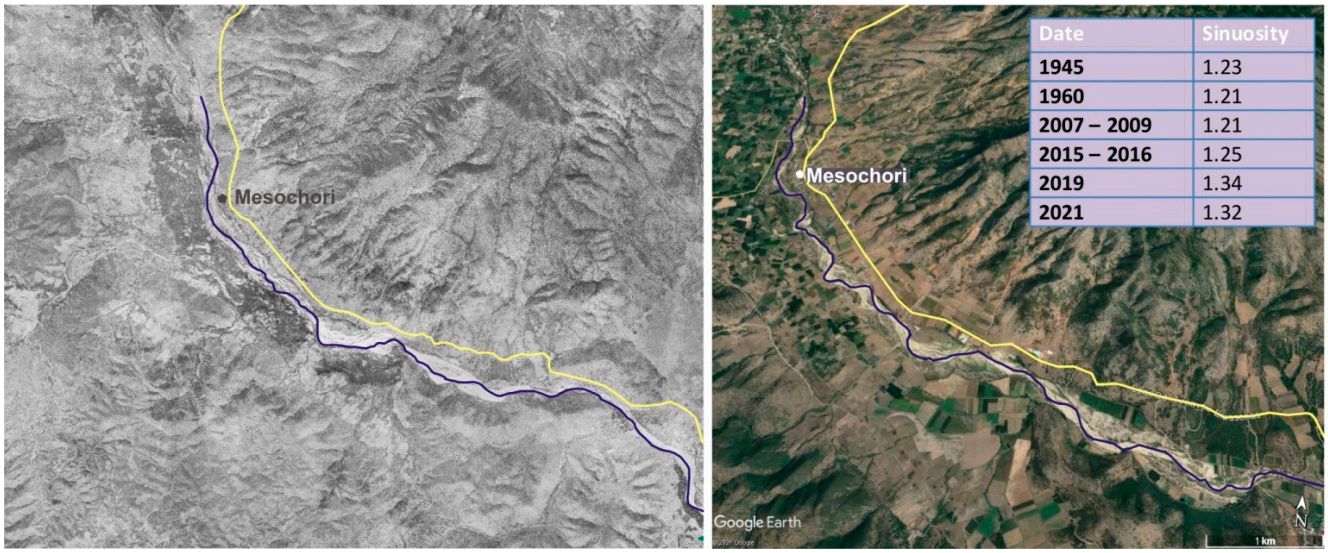

Figure 16. Change in sinuosity ratio of the Titarissios River (blue line) between 1945 and 2021.

4. Discussion

Analysis of differential interferograms certainly contributed to the rapid and detailed mapping of the ground deformation pattern of the March 3rd mainshock and its major aftershocks (Figure 4). At a first glance, the satellite approach suggests a mainly blind sliding structure [26]. However, the immediate post-event fieldwork observations with the support of drone surveys carried out in key areas documented that other tectonic structures were also reactivated to produce observable morphotectonic features. In particular, detailed field survey investigations provide evidence that deformation in the epicentral area is associated with an array of previously mapped normal faults considered as possibly active [7], though not included in the Greece database of seismogenic sources (GreDaSS; [44]). Also, the fieldwork allowed the recognition of new structures and confirmed their activity; among them are the Vlachogianni (VF) and Mesochori (MF) faults. Indeed, these tectonic structures show geomorphic features attesting to the geologically ongoing deformation; for example, they maintain straight mountain fronts, form well preserved triangular facets, and probably control the sinuosity of a central reach of the Titarissios River. In line with these observations and complementary to the overall picture are the dense network of liquefaction features, the minor rockfalls along these fault traces, and especially, the coseismic ground ruptures (Figures 2, 3, 6 and 8–13).

Similar partially contradicting results between DInSAR analyses and field evidence in seismogenic areas characterized by complex geological and tectonic settings are not exceptional [45–47]. In particular, the loss of coherence of the interferograms across areas covered by a significant thickness of loose sediments, as it occurs within the Titarissios Valley, clearly obscures the true pattern of the fringes. In the Thessalian case, if the amount of surface displacement on the antithetic VF and MF was comparable, as it seems to be confirmed by the field observations (Figures 7 and 10), the fringes outside the narrow Titarissios Valley graben should be not markedly displaced.

On the other hand, DInSAR results suggest that a significant amount of the coseismic slip occurred on a low-angle blind fault (e.g., [26]). To explain and combine all the available field and satellite observations, we suggest the occurrence of a complex tectonic structure within the uppermost part of the crust. The Vlachogianni Fault represents a steeply dipping shallow segment that reaches the Earth's surface as a splay of a low-angle normal fault at depth. If this is the case, the VF could have caused widespread subsidence on both its hanging-wall and footwall blocks (e.g., [48,49]). In this geometric-kinematic frame, the Mesochori Fault represents a major antithetic splay of the lowangle VF segment. In this regard, the palaeoseismological results could possibly provide evidence of whether

coseismic reactivations comparable to the March 2021 Damasi event occurred in the recent past along the MF. Further investigations are in progress and will likely shed light on this issue.

During the fieldwork, we mapped an array of cracks along the Damasouli Fault (DaF) and triangular facets along the Megalo Eleftherochori Fault (MeF) as well, both characterized by an N-S trend. A similar trend is also defined for the Kalivia Fault (Figure 2). These three structures are assumed as inherited ones, but it is tentatively considered that they could have played a secondary role during seismogenesis. These N-S trending faults possibly induced partitioning of the deformation or halted the rupture process across the dominating NNE-dipping structures; for example, the Vlachogianni Fault (VF).

5. Concluding Remarks

With documentation completed for (i) the recent activity of at least three faults and (ii) the clear westwards migration of the seismicity as emphasized in the interferogram analyses (e.g., [38] and this study; Figure 4), we can sum up with the following major conclusions:

(1) This study demonstrates the presence of a complex continuous fault array characterizing the epicentral area of the Damasi earthquake. In the epicenter, the fault array includes reactivated NNE to NE- or SSW to SW-dipping faults, and N-S trending inherited structures likely play a secondary role in the seismogenesis.
(2) The faults with a morphological expression within the area trend WNW-ESE, and are characterized by linear fault scarps and well-exposed triangular facets, indicating long-term deformation. The Titarissios River sinuosity possibly reflects short term deformation before the recent seismicity.
(3) The documented recent activity of these faults confirms that the Tyrnavos Graben was representing a seismic gap [7] in Central Greece and suggests that the tectonic basin is still growing and propagating westwards. Accordingly, the specific role of the Vlachogianni (VF) and Mesochori (MF) Faults was previously underestimated.
(4) The VF and MF control a minor graben structure that resembles the embryonic stage of the Tyrnavos Graben's recent westward propagation.

Author Contributions: Conceptualization, I.K.K., K.G.N., R.C.; data curation, I.K.K., K.G.N., A.K., R.C., A.B., V.Z., D.A.; formal analysis, I.K.K., K.G.N., R.C.; methodology, I.K.K., K.G.N., R.C.; software, K.G.N., A.K.; validation, I.K.K., K.G.N., V.Z.; visualization, I.K.K., K.G.N., A.K., R.C., A.B., V.Z., S.V., D.A., I.T.; writing—original draft, I.K.K., K.G.N., A.K., R.C., V.Z., S.V., D.A.; writing—review & editing, I.K.K., K.G.N., R.C. All authors have read and agreed to the published version of the manuscript.

Funding: This research received no external funding.

Data Availability Statement: Data available on request due to restrictions. The data presented in this study are available on request from the corresponding author. The data are not publicly available due to public safety reasons.

Conflicts of Interest: The authors declare no conflict of interest.

References

1. Koukouvelas, I.K. Geology of Greece. In *Liberal Books*; Athens Publishing: Athens, Greece, 2019; p. 343.
2. Doutsos, T.; Pe-Piper, G.; Boronkay, K.T.; Koukouvelas, I. Kinematics of the Central Hellenides. *Tectonics* **1993**, *12*, 936–953. [CrossRef]
3. Doutsos, T.; Koukouvelas, I.K.; Xypolias, P. A new orogenic model for the External Hellenides. *Geol. Soc. Lond. Spec. Publ.* **2006**, *260*, 507–520. [CrossRef]
4. Caputo, R. *Geological and Structural Study of the Recent and Active Brittle Deformation of the Neogene-Quaternary Basins of Thessaly (Central Greece)*; Aristotle University of Thessaloniki: Thessaloniki, Greece, 1990.
5. Doutsos, T. Postalpine geodynamik thessaliens (Griechenland). *Z. Dtsch. Geol. Ges.* **1980**, *131*, 685–698.
6. Caputo, R. Morphotectonics and kinematics along the Tyrnavos Fault, Northern Larissa Plain, Mainland Greece. In *Neotectonics and Active Faulting*; Stewart, I., Vita-Finzi, C., Owen, L.A., Eds.; G. Borntraeger: Stuttgart, Germany, 1993.

7. Caputo, R. Inference of a seismic gap from geological data: Thessaly (Central Greece) as a case study. *Ann. Geophys.* **1995**, *38*. [CrossRef]
8. Caputo, R.; Pavlides, S. Late Cainozoic geodynamic evolution of Thessaly and surroundings (central-northern Greece). *Tectonophysics* **1993**, *223*, 339–362. [CrossRef]
9. Caputo, R.; Helly, B. The Holocene activity of the Rodià Fault, Central Greece. *J. Geodyn.* **2005**, *40*, 153–169. [CrossRef]
10. Kokkalas, S.; Xypolias, P.; Koukouvelas, I.; Doutsos, T. Postcollisional contractional and extensional deformation in the Aegean region. In *Postcollisional Tectonics and Magmatism in the Mediterranean Region and Asia*; Dilek, Y., Pavlides, S., Eds.; Geological Society of America: Boulder, CO, USA, 2006; Volume 409, pp. 97–123.
11. Tsodoulos, I.M.; Stamoulis, K.; Caputo, R.; Koukouvelas, I.; Chatzipetros, A.; Pavlides, S.; Gallousi, C.; Papachristodoulou, C.; Ioannides, K. Middle-Late Holocene earthquake history of the Gyrtoni Fault, Central Greece: Insight from optically stimulated luminescence (OSL) dating and paleoseismology. *Tectonophysics* **2016**, *687*, 14–27. [CrossRef]
12. Caputo, R.; Bravard, J.-P.; Helly, B. The Pliocene-Quaternary tecto-sedimentary evolution of the Larissa Plain (Eastern Thessaly, Greece). *Geodin. Acta* **1994**, *7*, 57–85. [CrossRef]
13. Caputo, R.; Helly, B.; Rapti, D.; Valkaniotis, S. Late Quaternary hydrographic evolution in Thessaly (Central Greece): The crucial role of the Piniada Valley. *Quat. Int.* **2021**, in press. [CrossRef]
14. Caputo, R.; Helly, B.; Pavlides, S.; Papadopoulos, G. Palaeoseismological investigation of the Tyrnavos Fault (Thessaly, Central Greece). *Tectonophysics* **2004**, *394*, 1–20. [CrossRef]
15. Caputo, R.; Helly, B. The European palaeoseismological museum of Tyrnavos, Central Greece. *Geophys. Res. Abstr.* **2007**, *9*, 283.
16. Caputo, R.; Piscitelli, S.; Oliveto, A.; Rizzo, E.; Lapenna, V. The use of electrical resistivity tomographies in active tectonics: Examples from the Tyrnavos Basin, Greece. *J. Geodyn.* **2003**, *36*, 19–35. [CrossRef]
17. Caputo, R.; Hinzen, K.-G.; Liberatore, D.; Schreiber, S.; Helly, B.; Tziafalias, A. Quantitative archaeoseismological investigation of the Great Theatre of Larissa, Greece. *Bull. Earthq. Eng.* **2011**, *9*, 347–366. [CrossRef]
18. Caputo, R. The Rodia Fault: An active complex shear zone (Larissa Basin, Central Greece). *Bull. Geol. Soc. Greece* **1993**, *28*, 447–456.
19. Caputo, R. Ground effects of large morphogenic earthquakes. *J. Geodyn.* **2005**, *40*, 113–118. [CrossRef]
20. Papazachos, B.; Papazachou, C. *The Earthquakes of Greece*, 2nd ed.; Editions ZITI: Athens, Greece, 1997; 304p.
21. Caputo, R.; Helly, B. Archaeological evidences of past earthquakes: A contribution to the SHA of Thessaly, Central Greece. *J. Earthq. Eng.* **2005**, *9*, 199–222. [CrossRef]
22. Papastamatiou, D.; Mouyaris, N. The earthquake of 30 April 1954, in Sophades (Central Greece). *Geophys. J. R. Astron. Soc.* **1986**, *87*, 885–895. [CrossRef]
23. Papadopoulos, G.A. Rupture zones of strong earthquakes in the Thessalia region, Central Greece. *Boll. Geofis. Teor. Appl.* **1992**, *35*, 363–374.
24. Ambraseys, N.N.; Jackson, J.A. Seismicity and associated strain of central Greece between 1890 and 1988. *Geophys. J. Int.* **1990**, *101*, 663–708. [CrossRef]
25. Papazachos, B.C.; Panagiotopoulos, D.G.; Tsapanos, T.M.; Mountrakis, D.M.; Dimopoulos, G.C. A study of the 1980 summer seismic sequence in the Magnesia region of Central Greece. *Geophys. J. R. Astron. Soc.* **1983**, *75*, 155–168. [CrossRef]
26. Lekkas, E.; Agorastos, K.; Mavroulis, S.; Kranis, C.; Skourtsos, E.; Carydis, P.; Gogou, M.; Katsetsiadou, K.-N.; Papadopoulos, G.; Triantafyllou, I.; et al. The early March 2021 Thessaly Earthquake Sequence. *Newsl. Environ. Disaster Crises Manag. Strateg.* **2021**, *3*. [CrossRef]
27. Ganas, A.; Valkaniotis, S.; Briole, P.; Serpetisdakis, A.; Kapetanidis, V.; Karasante, I.; Kassaras, I.; Papathanassiou, G.; Karamitros, I.; Tsironi, V.; et al. Domino-style earthquakes along normal faults in Northern Thessaly (Greece): Kinematic evidence from field observations, seismology, SAR interferometry and GNSS. *Bull. Geol. Soc. Greece* **2021**, in press.
28. Nikolakopoulos, K.; Kavoura, K.; Depountis, N.; Kyriou, A.; Argyropoulos, N.; Koukouvelas, I.; Sabatakakis, N. Preliminary results from active landslide monitoring using multidisciplinary surveys. *Eur. J. Remote Sens.* **2017**, *50*, 280–299. [CrossRef]
29. Koukouvelas, I.K.; Nikolakopoulos, K.G.; Zygouri, V.; Kyriou, A. Post-seismic monitoring of cliff mass wasting using an unmanned aerial vehicle and field data at Egremni, Lefkada Island, Greece. *Geomorphology* **2020**, *367*, 107306. [CrossRef]
30. Kyriou, A.; Nikolakopoulos, K.; Koukouvelas, I.K.; Lampropoulou, P. Repeated UAV campaigns, GNSS measurements, GIS, and petrographic analyses for landslide mapping and monitoring. *Minerals* **2021**, *11*, 300. [CrossRef]
31. Massonnet, D.; Rossi, M.; Carmona, C.; Adragna, F.; Peltzer, G.; Feigl, K.; Rabaute, T. The displacement field of the Landers earthquake mapped by radar interferometry. *Nature* **1993**, *364*, 138–142. [CrossRef]
32. Massonnet, D.; Feigl, K.L. Satellite radar interferometric map of the coseismic deformation field of the M D 6.1 Eureka Valley, California earthquake of 17 May 1993. *Geophys. Res. Lett.* **1995**, *22*, 1541–1544. [CrossRef]
33. Peltzer, G.; Rosen, P. Surface displacement of the 17 May 1993 Eureka Valley, California, earthquake observed by SAR interferometry. *Science* **1995**, *268*, 1333–1336. [CrossRef] [PubMed]
34. Meyer, B.; Armijo, R.; de Chabalier, J.B.; Delacourt, C.; Ruegg, J.C.; Acache, J.; Briole, P.; Papanastassiou, D. The 1995 Grevena (northern Greece) earthquake: Fault model constrained with tectonic observations and SAR interferometry. *Geophys. Res. Lett.* **1996**, *23*, 2677–2680. [CrossRef]
35. Wright, T.J.; Parsons, B.E.; Jackson, J.A.; Haynes, M.; Fielding, E.J.; England, P.C.; Clarke, P.J. Source parameters of the 1 October 1995 Dinar (Turkey) earthquake from SAR interferometry and seismic body wave modelling. *Earth Planet. Sci. Lett.* **1999**, *172*, 23–37. [CrossRef]

36. Burgmann, R.; Rosen, P.; Fielding, E. Synthetic aperture radar interferometry to measure Earth's surface topography and its deformation. *Ann. Rev. Earth. Planet. Sci.* **2000**, *28*, 169–209. [CrossRef]
37. Funning, G.J.; Garcia, A. A systematic study of earthquake detectabilityusing Sentinel-1 interferometric wide-swath data. *Geophys. J. Int.* **2019**, *216*, 332–349.
38. Tolomei, C.; Caputo, R.; Polcari, M.; Famiglietti, N.A.; Maggini, M.; Stramondo, S. The use of interferometric synthetic aperture radar for isolating the contribution of major shocks: The case of the march 2021 Thessaly, Greece, seismic sequence. *Geosciences* **2021**, *11*, 191. [CrossRef]
39. Goldstein, R.M.; Werner, C.L. Radar interferogram phase filtering for geophysical applications. *Geophys. Res. Lett.* **1998**, *25*, 4035–4038. [CrossRef]
40. Antoniadis, P.; Zeppos, I.; Gentzis, T. A preliminary study of the geology of the elassona lignite deposits in Central Greece. *Energy Sources* **2003**, *5*, 383–393. [CrossRef]
41. Pe-Piper, G.; Doutsos, T.; Boronkay, K. Structure, geochemistry and mineralogy of Hercynian granitoid rocks of the Verdikoussa area, Northern Thessaly, Greece and their regional significance. *Neues Jahrb. Mineral. Abh.* **1993**, *165*, 267–296.
42. Wallace, R.E. Geometry and rates of change of fault-generated range fronts, north-central Nevada. *J. Res. U.S. Geol. Surv.* **1978**, *6*, 637–650.
43. Hack, J.T. Stream profile analysis and stream gradient index. *J. Res. U.S. Geol. Surv.* **1973**, *1*, 421–429.
44. The Greece Database of Seismogenic Sources (GreDass). 2013. Available online: http://gredass.unife.it/ (accessed on 25 July 2021).
45. Rigo, A.; Chabalier, J.; Meyer, B.; Armijo, R. The 1995 Kozani-Grevena (Northern Greece) earthquake revisited: An improved faulting model from synthetic aperture radar interferometry. *Geophys. J. Int.* **2004**, *157*, 727–736. [CrossRef]
46. Kobayashi, T.; Tobita, M.; Koarai, M.; Okatani, T.; Suzuki, A.; Noguchi, Y.; Yamanaka, M.; Miyahara, B. InSAR-derived crustal deformation and fault models of normal faulting earthquake (M_j 7.0) in the Fukushima-Hamadori area. *Earth Planets Space* **2012**, *64*, 15. [CrossRef]
47. Wang, Y.; Lin, Y.N.N.; Simons, M.; Tun, S.T. Shallow rupture of the 2011 Tarlay earthquake (Mw 6.8), Eastern Myanmar. *Seismol. Soc. Am. Bull.* **2014**, *104*, 2904–2914. [CrossRef]
48. Forsyth, D.W. Finite extension and low-angle normal faulting. *Geology* **1992**, *20*, 27–30. [CrossRef]
49. Fernández-Blanco, D.; de Gelder, G.; Lacassin, R.; Armijo, R. Geometry of flexural uplift by continental rifting in corinth, Greece. *Tectonics* **2020**, *39*, 5685. [CrossRef]